Metals

Constitutive properties and plastic instabilities in the heat-affected zones of advanced high-strength steel spot welds

H. Rezayat[1,*] , H. Ghassemi-Armaki[2] , S. P. Bhat[2] , S. Sriram[2] , and S. S. Babu[1,3]

[1] Mechanical, Aerospace and Biomedical Engineering, University of Tennessee – Knoxville, Knoxville, TN 37916, USA
[2] Automotive Product Research, ArcelorMittal Global R&D, East Chicago, IL 46312, USA
[3] Manufacturing Demonstration Facility, Oak Ridge National Laboratory, Oak Ridge, TN 37831, USA

ABSTRACT

Recent publications have shown that the load-bearing capability of advanced high-strength steel (AHSS) spot welds do not scale linearly with the tensile strength of the base metal. Although this unexpected degradation of welds has been linked to the tempering of the martensite phase in the heat-affected zone (HAZ), the detailed elastic–plastic stress–strain behavior in different regions of the HAZ has not been reported. In this research, the plastic flow behavior in samples subjected to simulative weld thermal cycles with peak temperatures (T_{Peak}) ranging from 350 to 1250 °C was evaluated. Results from this study showed that the microstructural changes in the HAZ could result in large mechanical heterogeneity in AHSS spot welds. In addition, plastic instability in the form of yield point phenomena was observed. The yield point phenomena in these simulated HAZ samples, in contrast to base metal samples, were confirmed by the observation of Lüders band and stress fluctuations before the onset of strain hardening using digital image correlation. The local plastic instability was correlated to the chemical composition of the steel, initial microstructure, and thermal cycle. The Lüders front velocity maps revealed heterogeneous nucleation and growth of multiple Lüders bands with different front speeds. Interestingly, inter-critical ($Ae_1 < T_{Peak} < Ae_3$) HAZ samples show minimum yield strength even though the maximum softening occurs in the subcritical HAZ ($T_{Peak} < Ae_1$) samples.

Introduction

Advanced high-strength steels (AHSS) are produced with carefully selected chemical composition and precisely controlled thermomechanical processing. Their ultimate tensile strength ranges from 550 MPa and reaches up to 2000 MPa and is related to underlying microstructures with different fractions of ferrite, martensite, and austenite. These properties lead to improved safety, robust performance, and most importantly reducing the weight and achieving higher fuel economy, and hence emissions reduction [1] in the transportation industries. In the vehicle manufacturing process, resistance spot welding (RSW) is the most commonly used joining method to assemble stamped components to form the body structure. Thus, from a steel-grade design perspective it is very important to ensure that the designed product has a good combination of strength, ductility, and spot weldability. Steel manufacturers put considerable effort in the design and processing of new steels to ensure satisfactory weldability in addition to meeting the requirements for basic mechanical properties and surface characteristics.

For several grades of AHSS, heat-affected zone (HAZ) softening has been reported by many researchers [2–7]. Biro et al. [5] investigated the softening kinetics of the HAZ regions of dual-phase (DP) steels through thermal simulation of base metal samples. In their research, thermal cycles at different locations were described by Biro et al. [5], using the methodology introduced by Xia et al. [8]. The methodology developed by Xia et al. [8] is based on Rosenthal's heat transfer equations for two-dimensional cross sections. Biro's research on DP600 and DP780 steels revealed that during the welding, martensite decomposes into ferrite and cementite when subjected to thermal cycles typical to that of subcritical HAZ (i.e., peak temperatures below Ae_1). The extent of HAZ softening was confirmed with microhardness measurements. The effect of martensite fraction in the base metal on HAZ softening has been investigated by researchers like Xia et al. [8]. Their research showed that the extent of HAZ softening increased with higher base metal ultimate tensile strengths, in three different DP steels during laser welding with similar process parameters. The results suggest a linear relationship between the extent of HAZ softening and base metal martensite volume fraction [8, 9]. The above phenomenon was also validated by other researchers with nanoindenter measurements: A reduction in hardness was observed in regions containing martensite, while no change was observed in ferrite grains [6]. The extent of softening has been shown to be strongly related to the tempering temperature and increases with volume fraction of martensite in base metal (BM) [6, 8, 10]. It is not surprising because the tempering has little impact on the hardness of ferrite phase and the softening is more pronounced in the martensite [11].

Isothermal tempering kinetics of martensite is a well-known phenomenon discussed in the text books. However, the extension of these mechanisms to nonisothermal weld thermal cycles requires more attention [5, 8, 12, 13] due to changes in the driving force for nucleation of carbides and also diffusivity of carbon in the matrix [14] and therefore depends on the time spent at different temperatures. It has been reported [15] that the maximum softening occurs in the region close to, Ae_1, i.e., the temperature at which the incipient formation of new austenite is expected [15]. Low-temperature tempering and its effects on kinetics of phase transformation has been studied by several researchers [9, 16–20]. Similarly, and as a part of steel production, all DP and martensitic AHSS undergo a low-temperature tempering treatment with typical peak temperature of about 200 °C for a period of 90 s. During these conditions, clustering of carbon atoms to octahedral lattice sites and dislocations and the onset of transient carbides (ε-carbides) are expected. Therefore, any further tempering from welding thermal cycle may induce the formation of cementite (M_3C) [18–21]. The observation of carbides in the nugget region is often attributed to auto-tempering during the cool-down cycle of the welding due to recalescence effects [9, 19, 20]. Many of the published works above show that higher heat input leads to lower cooling rate, higher peak temperature, longer time for tempering, and henceforth higher magnitude of HAZ softening. The role of softening in the elastic–plastic deformation of steels has also been studied in the literature; for example, the strain localization and premature failure of the welded structure have been attributed to the softening of material in HAZ [22] of press hardened steel.

Recent researches on the new generation of AHSS [4, 23] have revealed a nonlinear relationship between the base metal tensile strength and that of the spot-welded samples when base metal tensile

strength exceeds 1000 MPa. These experimental results are extracted from the literature and are re-plotted in Fig. 1 and illustrate the nonlinearity of tension–shear performance above 1000 MPa. This behavior of traditional RSW joints in higher-strength AHSS with more complicated microstructures could be an impediment in using the new generation of AHSS. In our earlier attempts to rationalize the above phenomena through finite element method, the constitutive properties of different HAZ regions were scaled based on local hardness ratio [10, 24]. Using the extent of softening or hardening in the measured hardness values from the HAZ, the base material flow (stress–strain) behavior was scaled linearly. This scaling factor was assumed to be relevant to all characteristics including yield point, strain hardening exponent, and ultimate tensile strength. However, our sensitivity analyses of FEA simulations showed that such an assumption might lead to considerable uncertainty in the predicted performance of spot-welded structures.

The goal of this research is to understand the effects of spot welding process on the local deformation behavior of AHSS spot-welded samples. To answer this question, we investigated the local plastic flow of the simulated HAZ samples of a wide range of DP and martensitic AHSS using integrated tensile testing and digital image correlation technique. There is an emphasis on the instability behavior commonly known as discontinuous yielding before the onset of homogeneous plastic flow in the material and not on the instability following diffuse necking prior to
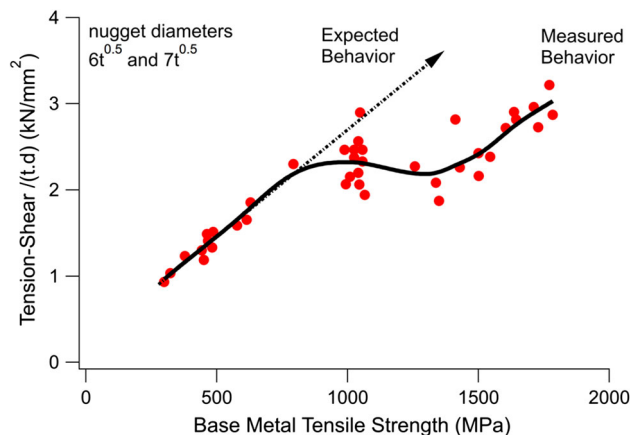
fracture. The results will provide guidance to computational modeling of spot-welded performance in the future and bridge the path from local microstructural evolutions to global deformation and fracture behavior for these welds.

Experimental procedure

Materials

Six grades of AHSS including four DP steels (DP590, DP980LC, DP980MC, and DP1180) and two martensitic steels (M1300 and M1700) were selected to represent a wide range of chemical composition, initial microstructure, and base metal tensile strength (see Tables 1, 2). The yield and tensile strength are based on the results from ASTM E8 standard for the sub-size specimen with a gauge length of 25 mm, as shown in Fig. 2. All the steels used in this study were secured from routine production coils that were tandem reduced and then processed on a water-quenched continuous annealing line. It is noteworthy that all the steels were subjected to a low-temperature tempering treatment with a peak temperature of about 200 °C for a period of 90 s during production. The martensite volume fraction (f_M) and its carbon content (C_M) in the dual-phase steels were estimated based on image processing and the rule of mixtures. In these calculations, to estimate the martensite carbon concentration, the ferrite carbon content was assumed to be 0.02 wt%. The equilibrium Ae_1 and Ae_3 phase transformation temperatures for each steel grade are calculated using JMatPro$^®$ and are summarized in Table 1.

Spot welding equipment and parameters

One set of spot-welded samples was prepared for each grade by welding sheets from the same grade and thickness (total of six samples for six grades of AHSS used in this study). Welding parameters were the same for all welds. A Taylor-Winfield 75–85 kVA, 60 HZ single phase, AC resistance spot welding machine was used. Type A 16 mm ISO 6.0 mm EFD electrodes were used with a water cooling system and 6 L/min water flow. Welding procedure sequence was as follows: squeeze (70 cycles); weld time (two pulses of 12 cycles with cooling of 2 cycles between cycles); and hold time (10 cycles). A constant

Figure 1 Comparison of measured tension–shear performance from spot welds made with DP and martensitic AHSS shows a nonlinear relationship between the spot weld strength and base metal strength.

Table 1 Chemical composition, martensite fraction, and phase transformation temperature of the investigated steels

Steel	Alloying elements (wt%)			C_M (wt%)	f_M (vol%)	Transformation temperature (°C)	
	C	Mn	Si			Ae_1	Ae_3
DP590	0.09	0.99	0.284	0.441	16	705	862
DP980LC	0.10	2.19	0.65	0.154	59	682	829
DP980MC	0.15	1.50	0.28	0.327	42	699	827
DP1180	0.14	2.07	0.64	0.17	81	691	822
M1300	0.19	0.39	0.15	0.19	100	723	844
M1700	0.31	0.47	0.19	0.31	100	725	812

Table 2 Tensile properties and hardness of the as-received AHSS used in this study

Steel	Thickness (mm)	YS (MPa)	UTS (MPa)	Total elongation (%)
DP590	1.5	390	636	23
DP980LC	1.4	710	1056	13
DP980MC	1.6	624	1025	13
DP1180	1.6	956	1266	11
M1300	1.4	1154	1386	6
M1700	1.6	1706	1876	5

Figure 2 Dimensions for the samples used in Gleeble simulations with the outline for the sample used in tensile testing. Tensile sample dimensions are according to ASTM E8 sub-size standard specimen.
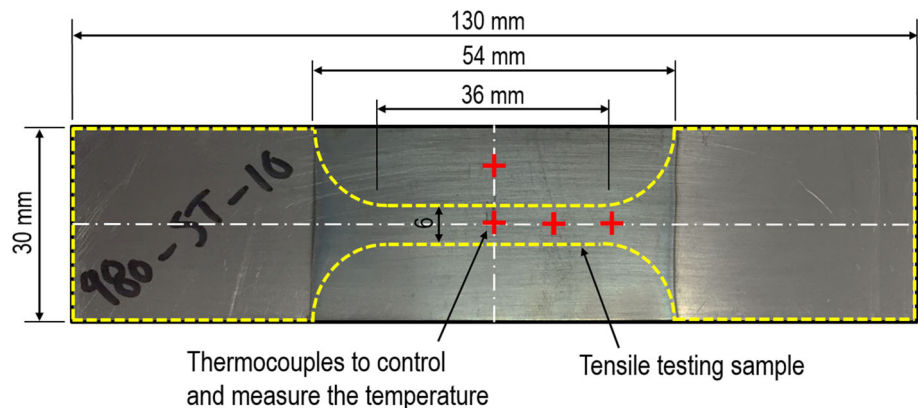
electrode load of 5 kN was used for all welds. The welding procedure, samples' geometry, and testing conditions were selected according to AWS D8.9 standards [25]. With these spot welding parameters, a final nugget diameter of 6 ± 0.4 mm was obtained, depending on the steel chemistry and the sheet thickness. These samples were used for local microstructure and hardness evaluations, and variation of nugget diameter among steels does not affect the results.

Prediction of thermal cycles and Gleeble thermal simulations

Because of the difficulties in direct measurement of temperature during spot welding, finite element (FE) method was used to obtain the local thermal cycles by simulating the spot welding process. These FE simulations were performed using SORPAS (by SWANTEC) on the same steel grades and sheet thickness. Six locations were selected within the HAZ region of the spot weld corresponding to peak temperatures of 350, 500, and 650 °C [i.e., subcritical HAZ (SCHAZ) below the Ae_1 temperature], 760 °C [i.e., inter-critical HAZ (ICHAZ), between Ae_1 and Ae_3] and two peak temperatures in upper-critical HAZ (UCHAZ); 950 °C corresponding to fine-grained HAZ (FGHAZ) and 1250 °C corresponding to coarse-grained HAZ (CGHAZ). Isothermal cycles equivalent to non-isothermal ones from FE simulations were used in a Gleeble-3800 thermomechanical simulator. Thermal histories for Gleeble simulations are presented in Fig. 3. From FE simulations only results for 650 °C and 1250 °C are shown, as
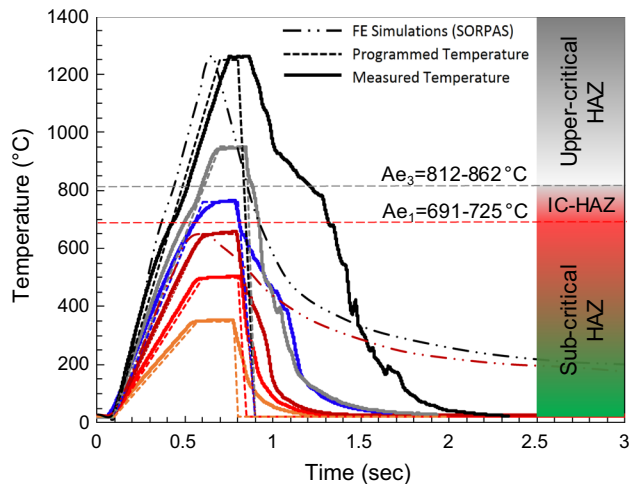
Figure 3 Overview of the programmed and measured thermal cycles used for simulating different regions of heat-affected zone in Gleeble® thermomechanical simulator. Note that we are not able to achieve rapid cooling rate in the experimental sample due to inherent thermal mass in the system.

examples and for comparisons. For the Gleeble simulations, 126 samples (6 steel grades × 3 repeats × 7 peak temperatures) were prepared from AHSS sheets. Tensile tests were performed on specimens with dimensions according to ASTM E8 standard with 25 mm gauge length and dimensions shown in Fig. 2.

The Gleeble samples were designed such that a uniform peak temperature was achieved in the gauge length of them. This was to ensure that a homogeneous material distribution exist in the gauge length of tensile testing samples. This methodology involved two steps: (1) During Gleeble simulations, four thermocouples were used to measure the temperature gradient in rolling and transverse directions (as shown in Fig. 2) (see "Appendix" for calibration method). The largest drop in peak temperature was measured to be 23 °C in rolling direction and place close to the grips. In transverse direction, temperature drop was negligible. (2) The hardness measurements were taken on the cross section of samples cut from Gleeble samples for checking the material homogeneity in gauge length and comparison with the spot-welded samples.

Microstructural characterization and microhardness measurements

Microstructure of the Gleeble and spot-welded samples was characterized using standard characterization techniques [26]. Microhardness measurements were taken by using a hardness tester with 300 g of load and 15 s dwell time on the cross section of both the spot welds and Gleeble simulated HAZ samples in the rolling direction, as per the ASTM E92 standard. The indent spacing was kept at 250 μm for all measurements, unless otherwise specified. Hardness measurements were used for following purposes: (1) to evaluate the local hardness and reveal the hardness heterogeneity throughout the spot-welded regions, (2) to distinguish different regions of spot-welded samples by comparing the hardness values and transitions, and (3) to calibrate the thermal cycles for the Gleeble thermal simulation as explained in "Appendix" section of this paper.

Tensile testing and digital image correlation technique

The MTS Criterion® C45 universal tensile testing frame was used to perform uniaxial tensile and tension–shear testing. The loading condition was set at a displacement rate of 2 mm/min for both types of tests. The tensile testing samples, extracted from the Gleeble samples, follow the ASTM E8 standard. For spatially resolved measurement of deformation and strain fields within the gauge length, a DIC system (manufactured by Correlation Solutions) was used. Following the procedures suggested by the manufacturer, the surface of samples was coated with prime white and dark speckle patterns on the surface. The VIC-2D image analysis software (Correlation Solutions) was used for post-processing the DIC data. A sampling rate of 10 Hz was used. A virtual extensometer with a length of 25 mm in gauge (along the sheet rolling direction) was used within the VIC-2D software to calculate the overall strains. With these measurements, the engineering and true stress–strain curves were described for different HAZ regions of all the steels. Tension–shear testing was also used to capture the typical deformation behavior in DP and martensitic steels. DP590 and M1700 spot-welded samples were made in concert with AWS D8.9 standard with nugget diameter of 8 mm for both samples. These steels represent the lower and upper ranges of martensite volume fraction and base metal strength, and the local and global deformation behavior and failure of them was of interest. After loading and failure, these samples were cut in the loading direction (same as the rolling direction) to

reveal the deformation behavior in different regions of welded samples with more details.

Experimental results

Results from tension–shear testing

Results from the tension–shear tests on DP590 and M1700 spot-welded samples are presented in Fig. 4a. In both samples the failure locations are identified as the regions that have been heated below Ae₃ phase transformation temperature of each steel. This identification was based on locally experienced peak temperatures predicted by finite element models, as well as the measured hardness values and their gradients from spot-welded samples. The nugget rotation and extent of deformations were significantly different in these two samples. DP590 spot weld shows larger rotation in nugget. In addition, in this sample the plastic deformation in regions close to failure was more pronounced in comparison with that in M1700. Although it is tempting to correlate the failures in M1700 to brittle failures expected in martensitic steels, careful analyses of the failed region showed localized deformation (see Fig. 4b, c). The above results confirm the need for correlation of local microstructural gradients in spot welds (see Fig. 4d) and its response to localized and global plastic deformations, as investigated in the following sections.

Typical local microstructure of spot welds

To understand the localized plastic deformation in M1700 spot welds, high-magnification images of microstructural heterogeneity before mechanical testing are presented in Fig. 5. In the as-received base metal of M1700 steel, a martensitic lath microstructure with fine carbides (bright imaging) was observed. This is indeed expected since the base metal undergoes a low-temperature tempering step during production. Results for the nugget of spot weld similarly showed a martensitic microstructure with fine carbides. The existence of fine carbide in this region can be attributed to auto-tempering due to recalescence effect (release of enthalpy of fusion) during weld cooling [9, 19, 20, 27]. The upper-critical HAZ (UCHAZ), including regions corresponding to peak temperatures of 950 °C (FGHAZ) and 1250 °C (CGHAZ), also contained martensite with some brightly imaging fine carbides. Perhaps the most interesting observation from the microstructural analysis is for ICHAZ. In this region, an aggregate of
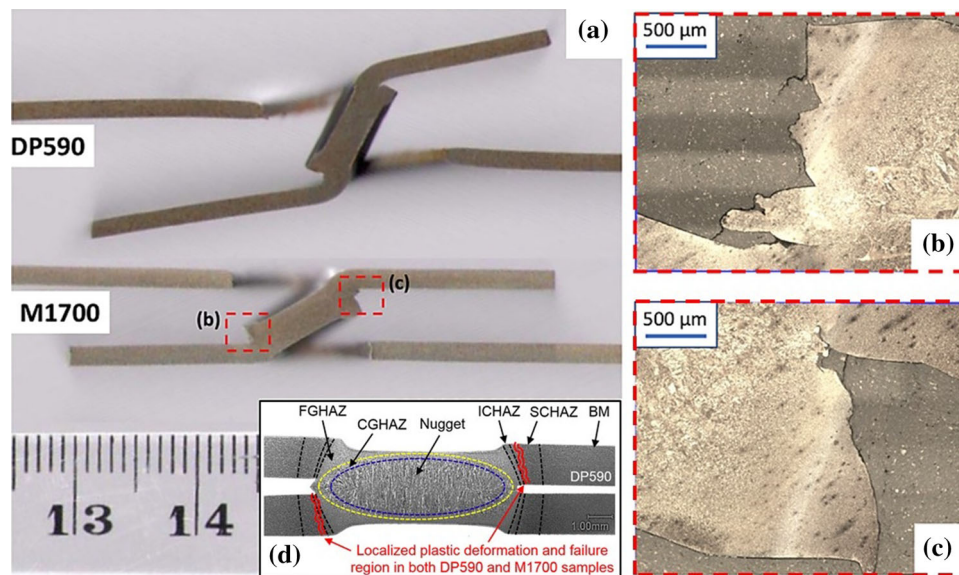

Figure 4 a Global deformation behaviors and failure in DP590 and M1700 tension–shear samples. Different extents of nugget rotation and global deformation can be observed (**a**). Localized plastic deformation in M1700 steels are marked in locations and are shown in high magnifications (**b, c**). Failures in both steels are correlated to regions with peak temperature below Ae3 based on comparing the location of failures with predicted thermal distributions from the FE simulations and hardness measurements as are schematically illustrated in (**d**) for the cross section of DP590 unloaded spot weld.
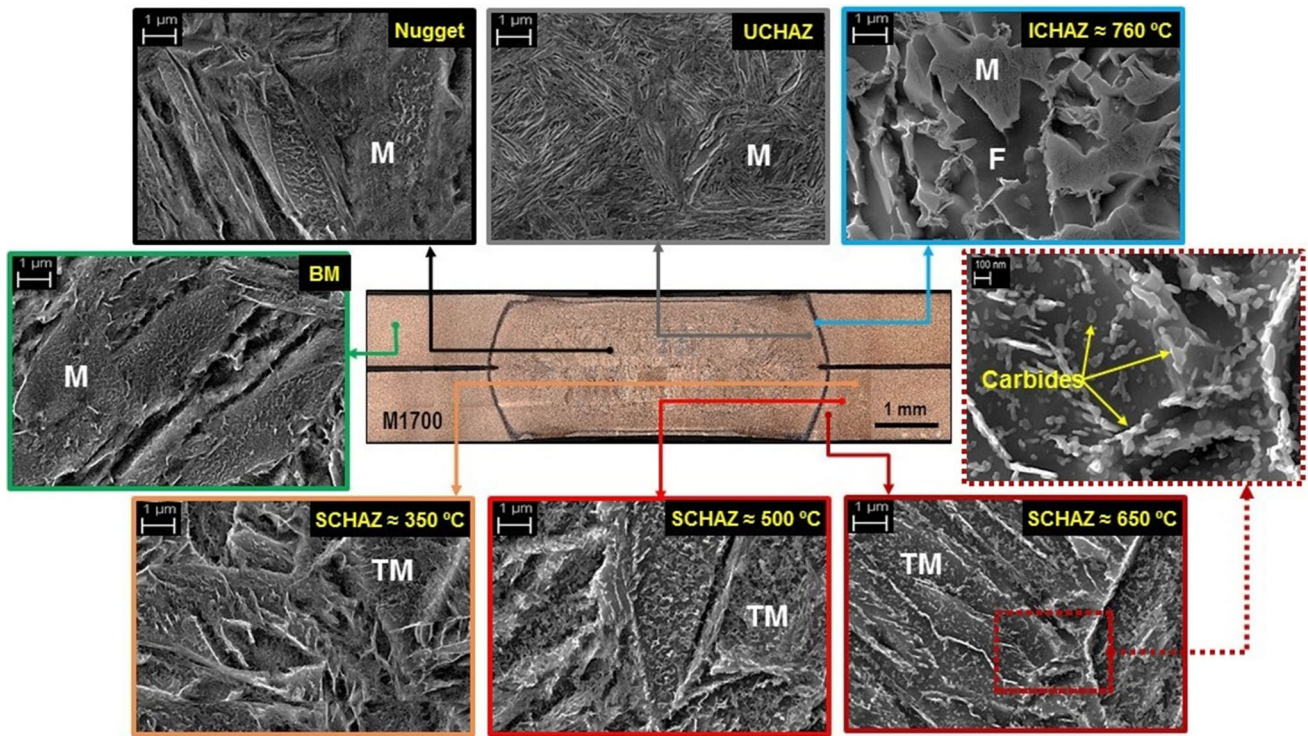
Figure 5 Overview of microstructural heterogeneity within the spot-welded sample made from M1700 AHSS obtained using scanning electron microscopy. The annotations are explained as follows: *M* martensite; *F* ferrite; and *TM* tempered martensite. Note that the identification of carbides is based on the contrast observed in the SEM images and also prior work.

ferrite and martensite phases was observed with the amount of the latter increasing as we move toward the fusion line. Although we cannot accurately assign the peak temperatures to different locations within the HAZ of spot welds, our interpretations of different regions are based on the etching response, high-magnification observation of microstructure, and also the measured hardness gradients (see Fig. 6). The widths of ICHAZ varied from 0.1 to 0.3 mm, depending on the chemistry and phase transformation temperatures of each steel. In the SCHAZ of dual-phase steels, ferrite and tempered martensite microconstituents were observed. In the case of martensitic steels, only tempered martensite was observed. In SCHAZ corresponding to lower peak temperatures (BM and lightly etching regions) cementite particles are finer and more dispersed, while in regions experiencing higher peak temperatures (darkly etching), the cementite particles are sparse and coarsened in martensite substructures and along the prior austenite grain boundaries. Based on the iso-surface temperature contours from FE analyses, the lightly etching regions should have experienced a peak temperature below 350 °C and the
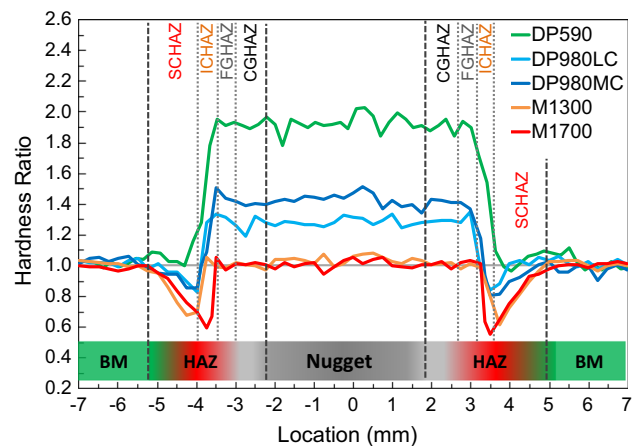

Figure 6 Hardness ratios along the diagonal line across the spot welds showing the hardness heterogeneity. Results show softening in SCHAZ and ICHAZ regions and hardening in UCHAZ and nugget. The base metal hardness for each steel is measured as: DP590: 199, DP980LC: 324, DP980MC: 311, M1300: 452, and M1700: 585 Vickers. Dashed lines show the approximate boundaries between regions of the spot welds.

darkly etching regions should have experienced peak temperatures ranging from 500 to 650 °C. Above identifications are phenomenological and must not be

considered as fact due to our inability to extract thermal signatures during welding. Therefore, we have used FE simulation results, hardness measurements, and microstructural features to correlate the local plastic deformation and failure to microstructures in the SCHAZ or ICHAZ regions. It is also noteworthy that these observations are not new and have been reported extensively in the literature [5–7, 12, 20, 28–31].

Microhardness examination of spot-welded samples

Results from microhardness measurements taken on the cross section of spot-welded samples are presented in Fig. 6. These results illustrate the existence of softening and hardening in the HAZ of all steels, however with different extents. The softening is observed in two regions of spot-welded samples: (1) in the SCHAZ of all the six steels of this study, with DP590 and M1700 possessing the maximum and minimum hardness ratios of 94% and 58%, respectively; (2) in the ICHAZ regions wherein minimum hardness value was similar to that of SCHAZ and experience peak temperatures were close to Ae_1. In ICHAZ an increase in hardness with an increase in the freshly formed martensite is observed. Interestingly, the above data also correlated with microhardness data measured from samples subjected to Gleeble thermal simulations. For example, the maximum hardness values were observed in the samples with two peak temperatures used in Gleeble simulations: 950 °C and 1250 °C corresponding to FGHAZ and CGHAZ, which correlates with martensite microstructure that forms within fine- and coarse-grained austenite grains in the spot welds, respectively.

Comparison of YS, UTS, and strain hardening exponent of Gleeble samples

Raw data from all tensile tests performed on Gleeble thermally simulated specimens are summarized in "Appendix" section of this paper. For comparative purposes, here we use the YS and UTS ratios and measure strain hardening exponents as shown in Figs. 7a, b and 8. The power-law equation ($\sigma = k\varepsilon^n$, with n as the strain hardening exponent) was used to obtain the average strain hardening exponent between the YS (stress at 0.2% plastic strain) and

UTS. Results presented in Fig. 7a show an increase in YS ratio for samples with T_{peak} = 350 °C, followed by a continuous decrease as T_{Peak} approaches the 650 °C, for DP steels. The trend is different for the fully martensitic steels (M1300 and M1700) in which a continuous reduction in YS ratio is observed. Interestingly, for both the DP and martensitic steels, the reduction in YS ratio continues to ICHAZ regions, where the T_{Peak} was 760 °C with values lower than that of SCHAZ regions for all steels. The DP590 and M1700 possess the minimum YS of 1.02 and 0.38, respectively, in the entire HAZ. By increasing the T_{Peak} and eventually going above the Ae_3, the YS increases in all steels. The maximum YS ratio was
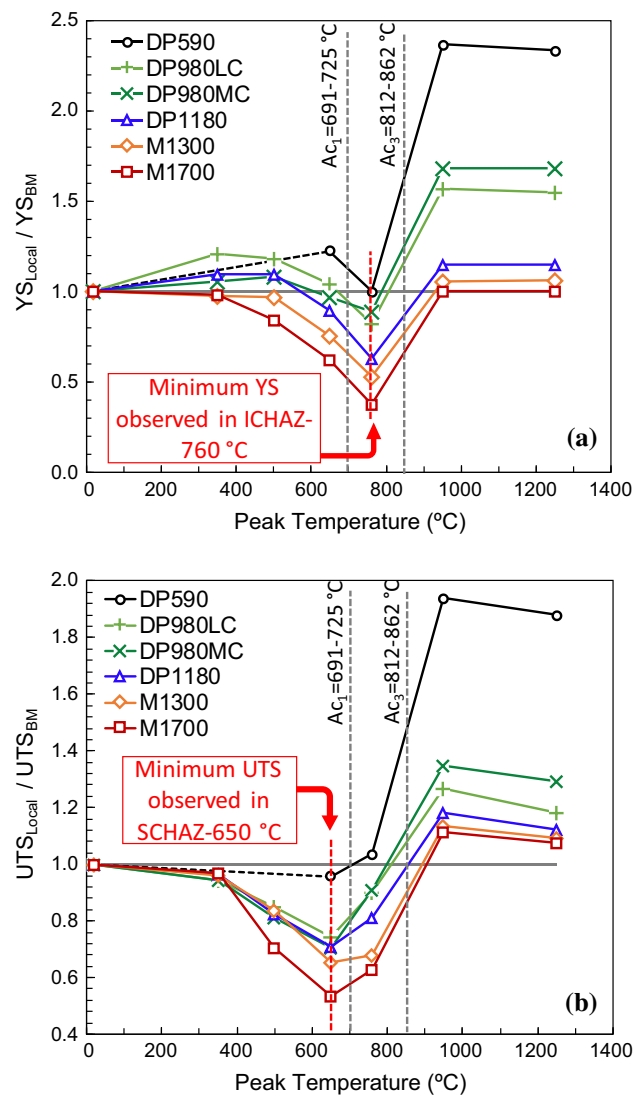

Figure 7 Variation of yield stress and ultimate tensile stress as a function of peak temperature obtained from Gleeble thermally simulated samples.
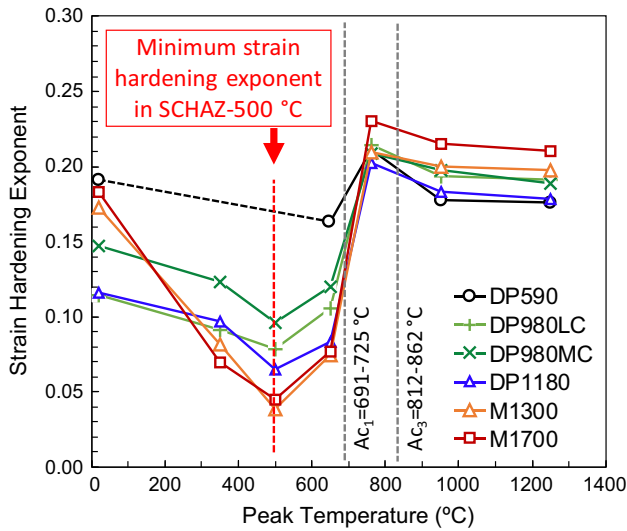
Figure 8 Variation of strain hardening exponent as a function of peak temperature obtained from Gleeble thermally simulated samples.

observed in UCHAZ with a peak temperature of 950 °C wherein the FGHAZ microstructure was observed from the microstructural analysis. The maximum and minimum YS ratios observed at T_{Peak} of 950 °C for DP590 and M1700 were 2.34 and 1, respectively.

Similar analyses were performed using the UTS ratios for all steels. Results shown in Fig. 7b confirm that the tensile strength in SCHAZ decreases with an increase in peak temperature and minimum UTS for all steels observed in SCHAZ at T_{Peak} of 650 °C. The minimum and maximum UTS ratios observed for DP590 and M1700 are 0.96 and 0.54, respectively. The maximum UTS observed for all steels with a peak temperature of 950 °C in the region where the fine-grained martensitic microstructure was observed from SEM analysis. The UTS ratio slightly decreases by moving from 950 °C toward 1250 °C peak temperature. The change in strain hardening exponent (n term in the flow curve equation $\sigma = k\varepsilon^n$) for steels subjected to different thermal cycles is shown in Fig. 8. Interestingly, the "n" values decreased to a minimum value of 0.04 for the all the samples subjected to thermal cycling at a peak temperature of 500 °C which corresponds to semi-perfect plastic behavior. The two fully martensitic steels (M1300 and M1700) show the largest drop in strain hardening despite the high strain hardening values in base

metal before thermal cycling. With the increase in peak temperature from 500 to 650 °C (belonging to SCHAZ) and then 760 °C (belonging to ICHAZ), the hardening exponent increases, with the highest value belonging to ICHAZ in all steels. The strain hardening shows a slight decrease with increasing peak temperature and by moving from the ICHAZ toward UCHAZ.
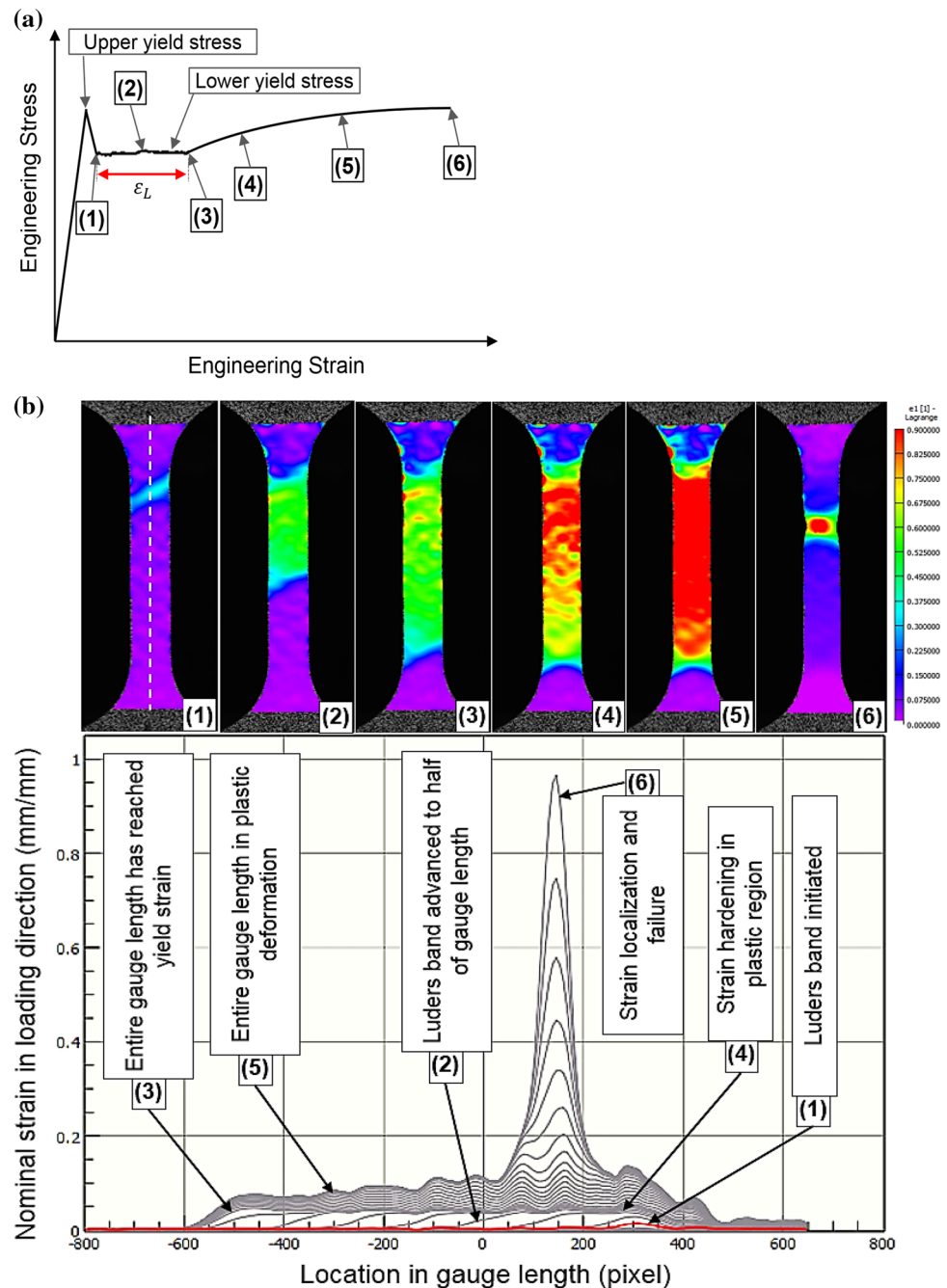
Observation of yield point phenomena

Discontinuous yielding in the form of yield point phenomena (YPP) with corresponding Lüders band was observed in thermally simulated samples for peak temperatures below Ae_1 (i.e., SCHAZ) in all the steels. The YPP is characterized by upper yield stress (UYS), lower yield stress (LYS), and Lüders strain (ε_L), as shown schematically in Fig. 9a. The interpretation of stress–strain curves with YPP is schematically illustrated in Fig. 9b with the spatial strain field calculated from DIC analysis of DP1180 steel subjected to thermal cycles with a peak temperature of 650 °C, as an instance. Figure 9b shows the Lüders strain initiation and propagation in the gauge length of the sample at different stages marked as (1), (2), and (3). With continued straining above the YPP, the strain hardening sets in and eventually leads to failure (Fig. 9b, 3–6).

Discussion

The primary focus of this paper is to investigate the effect of thermal cycles with different peak temperatures, similar to those in spot welding process, on the local constitutive properties of DP and martensitic advanced high-strength steels. In the previous section, the variations in plastic flow properties in terms of YS, UTS, and strain hardening exponents are summarized. The re-emergence of YPP and corresponding Lüders strain are also shown. Although previous researches are focused on the elastic–plastic properties of tempered DP and martensitic steels, all of them ignore the local mechanical heterogeneities in scales smaller than gauge length and the associated plastic instability. Therefore, in the following discussions, we initially discuss the material heterogeneity and then evaluate the details of plastic

Figure 9 Schematic representation of stress–strain curve for material with discontinuous yielding (**a**) and DIC images from Lüders band initiation and propagation in the gauge length and strain along the path in the loading direction for DP1180 Gleeble simulated HAZ sample tempered to 650 °C (**b**).

Heterogeneous plastic flow properties

Results presented in "Experimental results" section show that thermal cycles with different peak temperatures could lead to significant changes in local constitutive properties (YS, UTS, and hardening exponent) for thermally simulated samples that are simulative of local regions of spot welds. As these local microstructures influence deformation behavior and failure of AHSS spot welds the heterogeneity of elastic–plastic properties needs detailed analyses. Since the lowest values for YS and UTS ratios were measured from samples with peak temperatures of 760 and 650 °C for all steels, these regions can experience strain localization leading to lower strength and/or change in failure mode that is described in Fig. 1. Therefore, the discussions in this section will

instability. Finally, these characteristics will be correlated to the underlying microstructures.

be primarily focused on samples heated to these two peak temperatures. Figure 10 shows the YS and UTS ratios for different steels used in this study. As it can be seen, for all these steels (except DP590) and at these peak temperatures, the YS and UTS ratios are below one (except DP590 and DP980LC). This implies that the mechanical heterogeneities increase in higher grades of these steels. Another interesting observation is that the YS ratio in ICHAZ (at 760 °C) is lower than that in SCHAZ (at 650 °C) in all the steels. This result suggests that this region may be the initial site for the strain localization in spot welds. It is noteworthy that we have used only one peak temperature (760 °C) for reproduction of ICHAZ material and therefore we do not know whether this result is generic and applicable to other peak temperatures with different fractions of fresh martensite. At other temperatures, substantially above Ae_1 and reaching

Ae_3, the extent of the newly formed austenite is expected to increase by replacing the initial microstructure of the base metal. These continually varying fractions of ferrite (low carbon supersaturation with no carbides), tempered martensite (partial carbon supersaturation with carbides), and fresh martensite that forms from the austenite formed during reheating are bound to influence the overall strain partitioning between these constituent phases. Implications of these heterogeneous plastic properties will be explained later in this section, after detailed analyses of the spatial and temporal plastic instabilities observed in DIC.

Spatial and temporal variations of plastic instabilities

An important outcome of our experimental work is the observation of plastic instability, in the form of yield point phenomena, in samples with peak temperatures corresponding to SCHAZ regions ($< Ae_1$). As presented in "Experimental results" section, the YPP and corresponding Lüders strain were mainly observed in samples with peak temperatures corresponding to 500 and 650 °C and were negligible in samples with peak temperature of 350 °C. Figure 11 shows the effect of peak temperature on Lüders strain: The measured Lüders strain increases with the peak temperature and reaches the maximum in samples heated to a peak temperature of 650 °C for all the steels. The only exception to this observation is from DP980MC because there was no momentous
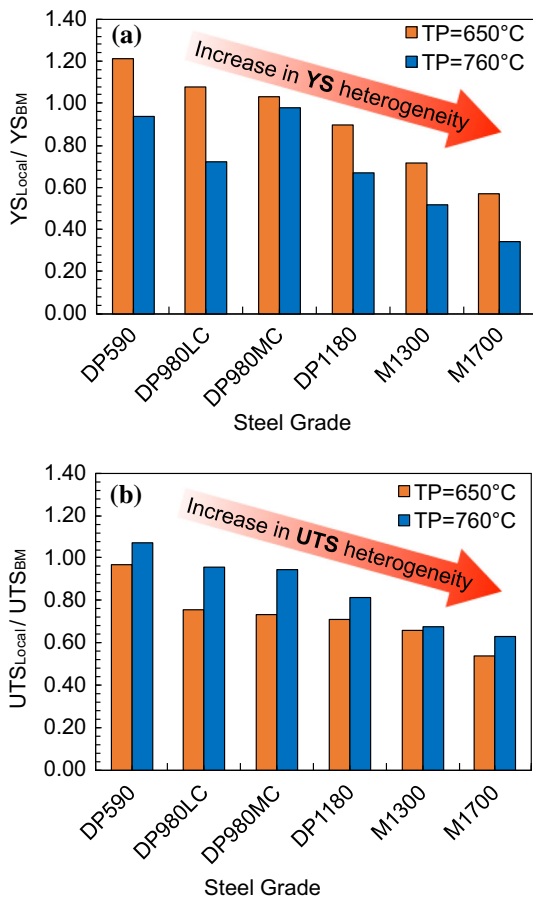

Figure 10 Plastic flow heterogeneity in HAZ of AHSS spot welds based on the results from tensile testing on thermally simulated samples. This heterogeneity increases in higher grades of these steels.
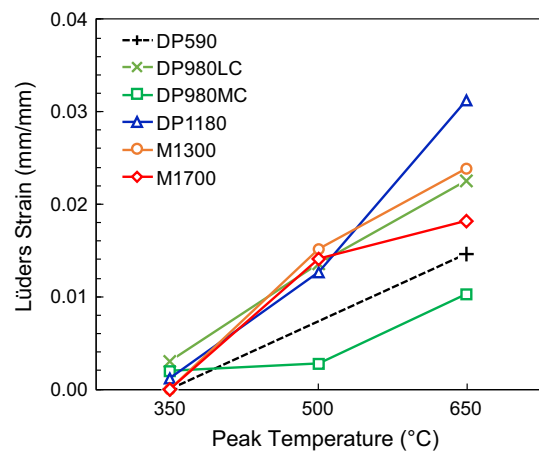

Figure 11 Lüders strain measured from Gleeble simulated SCHAZ samples. In all steels Lüders strain in SCHAZ increased with the thermal cycle peak temperature.

change in Lüders strain from samples heated to 350–500 °C. In contrast, DP1180 and DP980MC steels showed the largest and smallest Lüders strain at 650 °C, respectively. The Lüders strain can be correlated to the carbon content in the ferrite (BCC) or partially tempered martensite (BCC/BCT) lattice structures. This hypothesis was confirmed by correlations shown in Fig. 12, i.e., the Lüders strain of SCHAZ samples decreases with carbon concentration of martensite. The observation of YPP and Lüders strain and association only with samples of certain thermal cycles needs to be rationalized and will be the focus of the next section.

Results shown in Figs. 11 and 12 are based on DIC measurements from a 25 mm gauge length on the surface of tensile samples. Therefore, these values are average of the overall response of aggregated plastic flow that is happening at different rates across the whole gauge length. It is quite possible that the plastic flow properties at local levels can be different in regions containing varying mixtures of original ferrite, partially or fully tempered martensite, and newly formed martensite that have been produced during thermal cycling. By post-processing the strain field data obtained from DIC system using an in-house code that measures the speed of the Lüders band front during global loading of tensile samples and plotting the Lüders band velocity, we can get insight into the dynamics of nucleation and growth of plastic instabilities in gauge length of samples. Results from such analyses and at the strain value of 0.01 (to emphasize the Lüders strain) performed for DP590, DP980LC, and M1700 steel samples subjected
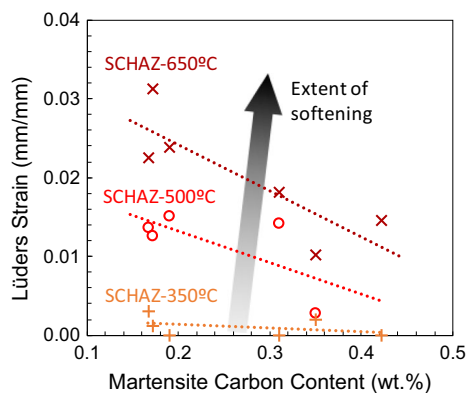
to thermal cycles with a peak temperature of 650 °C are shown in Fig. 13. The results from Lüders velocity contours show different behaviors. As it can be seen in M1700 sample, the number of Lüders band nucleation sites is significantly higher than that in DP980LC and then DP590. The Lüders velocity is also different with higher values belonging to M1700 and then DP980LC. This result confirms that the Lüders strain has different orientations with reference to loading axis, potentially due to spatial variation of the texture. Currently, such small-scale effects cannot be modeled using the finite element models and may require microstructure-/texture-based crystal plasticity models.

Overview of microstructural changes and rationalization of plastic instabilities

The kinetics of phase transformations of DP and martensitic steels during isothermal and non-isothermal thermal conditions, as well as their correlations to stress–strain behaviors has been extensively studied in the literature [2–9, 12, 13, 18–20, 27, 29, 32–51]. Based on the comprehensive review of the literature and computational models, we provide a schematic illustration of the microstructure evolution in six grades of steels during thermal cycling. The diagram is based on microstructure evolution in dual-phase steels (see Fig. 14). Similar evolutions are expected for the fully martensitic steels by considering only the martensite phase.

UCHAZ region

In this region, the steel is heated to single-phase austenite region and cooled rapidly to room temperature. This leads to the formation of fresh martensite from both fine and coarse austenite grains. These regions which are known as FGHAZ and CGHAZ have been studied extensively in the welding literature. Since the plastic instabilities were not observed in this region, rest of the discussions will focus only on the SCHAZ and ICHAZ regions.

SCHAZ region

In this region, the only microstructural change (see Fig. 14b) is related to continued tempering of the preexisting martensite. It is well known that this
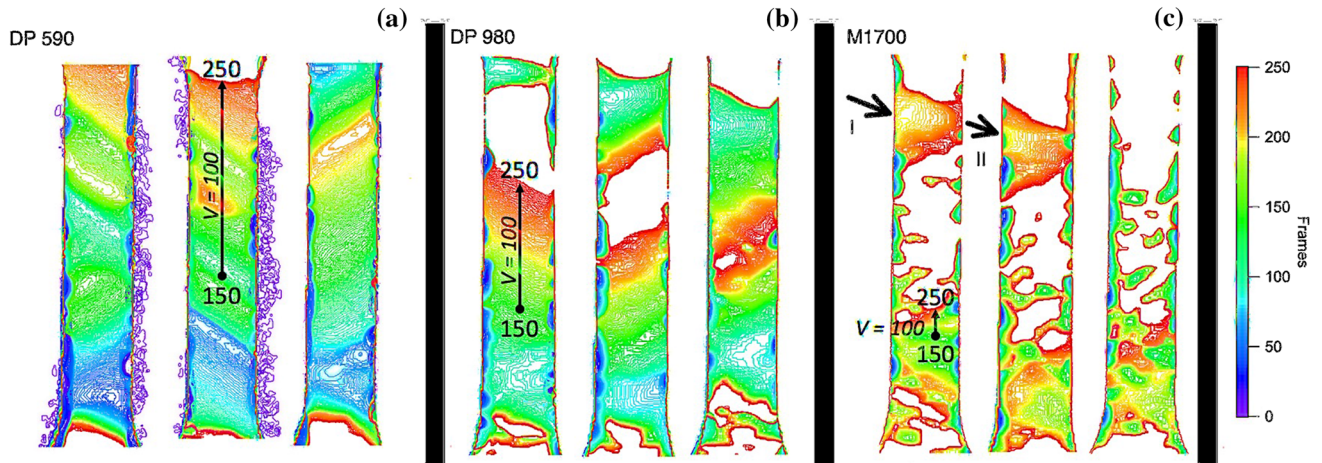

Figure 12 Lüders strain as a function of martensite carbon content and peak temperature in SCHAZ. Lüders strain shows an inverse correlation with martensite carbon content and increases with thermal cycle peak temperature.

Figure 13 Contour of localized strain trajectories for DP590, DP980LC, and M1700 samples, subjected to thermal cycles with a peak temperature of 650 °C, at strain of 0.01 and as a function of time. The Lüders band motion and numbers of initiation sites increase from DP590 to M1700. The rapid motion, multiple Lüders band initiation sites, and cross-width band motion are remarkably higher in M1700. Frames correspond to time intervals of 0.1 s.
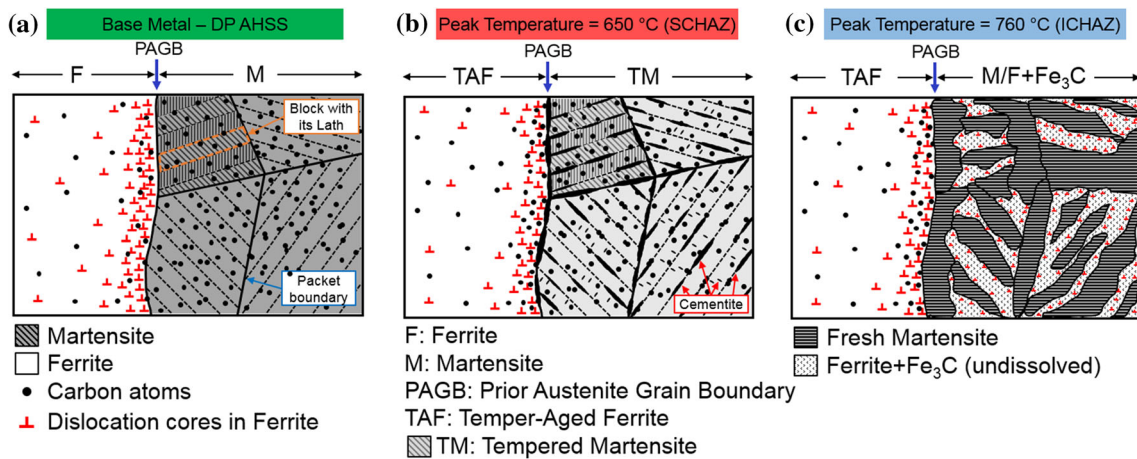

Figure 14 Simplified schematic illustration of microstructural evolutions occurring during thermal cycles of spot welding of DP AHSS with peak temperatures of 650 °C and 760 °C, corresponding to SCHAZ and ICHAZ, respectively. For the fully martensitic steels, events in martensite phase can be adopted, and therefore, no separate schematics are needed.

tempering reaction is accompanied by carbon clustering within the lattice or to the dislocations, growth of preexisting carbides, nucleation and growth of new carbides. Furthermore, a reduction in dislocation densities, formed during the original martensitic reaction before thermal cycling, is also expected. The extent of these reactions is dictated by thermal signatures that control the time spent at different temperatures below Ae_1.

ICHAZ region

In the ICHAZ, previously tempered martensite in the base metal transforms partially into austenite (see Fig. 14c) on heating above Ae_1. Due to rapid heating, short isothermal heating, and cooling cycles, the carbides in original tempered martensite are partially dissolved. On cooling down, this austenite transforms to fresh martensite. Due to the inherent difference in thermal expansion coefficient between ferrite and austenite, during the cooling and transformation of the austenite to martensite, stresses will be generated in the original tempered martensite or ferrite. These boundary conditions may induce the

geometrically necessary dislocations in the boundaries of original BM microstructure and freshly formed martensite. Similar to the other regions of HAZ, the extent of fresh martensite will be dictated by thermal signature, i.e., peak temperature and time spent above the Ae1 temperature.

Rationalization of yield point phenomenon

Emergence of yield point phenomenon is related to Cottrell atmosphere brought about by segregation of carbon and/or nitrogen to dislocations which pins the mobile dislocations and the onset of Lüders strain [52–58]. While the upper yield stress is related to the static pinning of dislocation by Cottrell atmosphere [52, 53], however, the rapid dislocation multiplication has been known to play a significant role in the Lüders band propagation and strain [54, 58, 59]. Both of these phenomena are strongly related to the carbon content and dislocation density of steels. The formation of Cottrell atmosphere has been shown to be strongly related to the amount of free carbon and mobile dislocation density in the microstructure and the interaction between these two [53, 55–58]. The observation of YPP in SCHAZ of fully martensitic steels of this study indicates that this phenomenon can happen in tempered martensite. Several studies have also shown that tempering supersaturated ferrite can also lead to the formation of Cottrell atmosphere and hence occurrence of YPP [54]. The carbon content of bcc iron can change as the peak temperature changes. This is shown in Fig. 15 based on the thermodynamics calculation using JMatPro® software, for equilibrium condition. Interestingly, the ferrite carbon content increases significantly, i.e., about ten times as the tempering temperature increases from 350 to 650 °C. This carbon remains in the bcc lattice upon rapid cooling cycles and can have pinning effects on the dislocations [53, 56]. Therefore, both the temper-aged ferrite and tempered martensite are responsible for the YPP in DP and martensitic steels.

With significant microstructural changes in SCHAZ (YPP was only observed in this region), the effect of tempering on both the ferrite (temper-aging) and martensite (tempering) and the amount of free carbon and mobile dislocation density have to be considered in a unified manner. Phenomenological models for the YPP can be used to study the variation of dislocation density in the microstructure. The
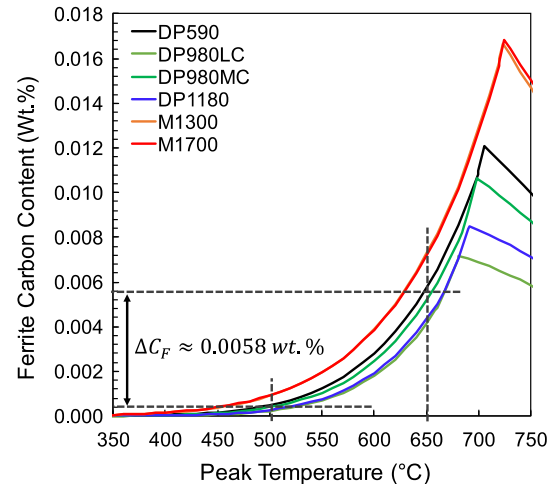

Figure 15 The amount of carbon that can dissolve in ferrite in equilibrium as a function of peak temperatures. Carbon solubility in ferrite increases with an increase in peak temperatures. Slight reduction above a maximum value at high temperatures above 700 °C is indeed expected due to the onset of the austenite formation.

model introduced by Hahn [58], as shown with its parameters in Fig. 16, is one model that uses the dislocation density as the main parameter for generating stress–strain curves with YPP. We used this model to generate the stress–strain curves corresponding to those obtained from tensile testing experiments. The corresponding curves for the tensile testing samples with the lowest and the highest YS are plotted in Fig. 16 along with curves for SCHAZ samples. The dislocation density for these two curves is also shown and indicates that the dislocation density in the steels microstructure changes due to the thermal cycles with different peak temperatures. Although these types of models formed based on fitting of experimental data can be used for other materials, however, due to numerous variables, there is no unique solution. Thus, this type of models cannot effectively represent the YPP for different size scales.

The above sensitivity analyses show that these two parameters (carbon and dislocation density) can vary remarkably in different peak temperatures and reflect on the plastic instabilities seen in the thermally simulated samples subjected to peak temperatures belonging to SCHAZ of DP and martensitic AHSS. The appearance of plastic instabilities and Lüders band in the mechanical behavior of the SCHAZ and ICHAZ regions may lead to high degree of
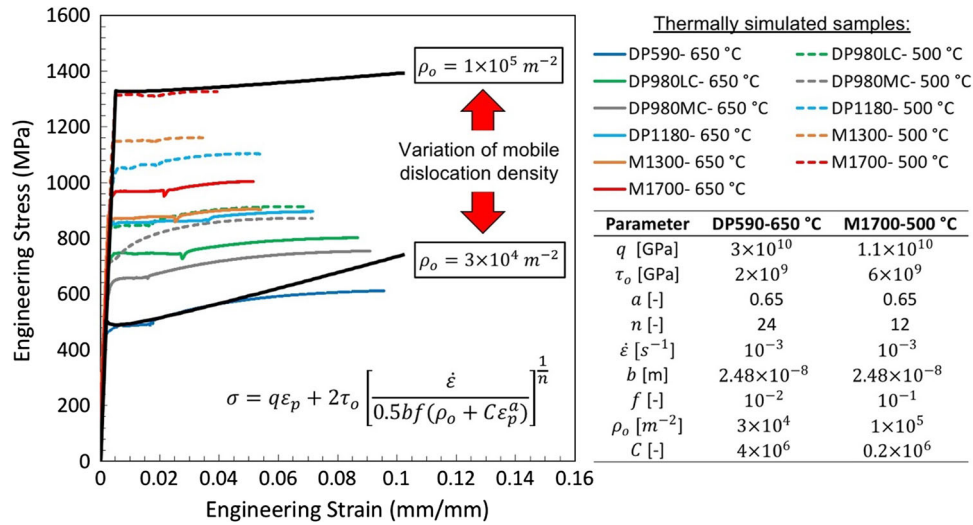
The figure contains a legend and table:

Thermally simulated samples:

DP590- 650 °C	DP980LC- 500 °C
DP980LC- 650 °C	DP980MC- 500 °C
DP980MC- 650 °C	DP1180- 500 °C
DP1180- 650 °C	M1300- 500 °C
M1300- 650 °C	M1700- 500 °C
M1700- 650 °C	

Parameter	DP590-650 °C	M1700-500 °C
q [GPa]	3×10^{10}	1.1×10^{10}
τ_o [GPa]	2×10^{9}	6×10^{9}
a [-]	0.65	0.65
n [-]	24	12
$\dot{\varepsilon}$ [s^{-1}]	10^{-3}	10^{-3}
b [m]	2.48×10^{-8}	2.48×10^{-8}
f [-]	10^{-2}	10^{-1}
ρ_o [m^{-2}]	3×10^{4}	1×10^{5}
C [-]	4×10^{6}	0.2×10^{6}

$\rho_o = 1\times10^{5}\ m^{-2}$

Variation of mobile dislocation density

$\rho_o = 3\times10^{4}\ m^{-2}$

$$\sigma = q\varepsilon_p + 2\tau_o \left[\frac{\dot{\varepsilon}}{0.5bf(\rho_o + C\varepsilon_p^a)}\right]^{\frac{1}{n}}$$

Figure 16 Variation of dislocation density based on fitting a phenomenological model proposed by Hahn [58]. In this model, σ is the plastic stress, q is the macroscopic work hardening coefficient, τ_o is the resolved shear stress, b is the Burgers vector, $\dot{\varepsilon}$ is the strain rate, ρ_o is the initial mobile dislocation density, f is the fraction of initially mobile dislocations, ε_p is the plastic strain, and a, C, and n are dislocation density parameters from experiments. A wide range of mobile dislocation density was used in the fittings.

uncertainties and plastic instabilities in the behavior of the AHSS spot welds.

Conclusions

The effect of thermal cycles with different peak temperatures due to spot welding process on the local constitutive properties and plastic instabilities of several DP and martensitic AHSS was investigated. The following conclusions can be made based on the results and analyses:

- Significant softening, in terms of hardness change, was observed in both SCHAZ and ICHAZ regions of spot-welded samples. The extent of softening was similar in these regions in areas close to Ae_1 phase transformation temperature of each steel. The lowest and highest extents of softening were observed in DP590 and M1700, with hardness ratios of 0.94 and 0.58, respectively.
- Interestingly, the minimum yield stress ratio (YS_{Local}/YS_{BM}) was observed in the ICHAZ regions heated to a peak temperature between Ae_1 and Ae_3 in all steels which may be the location for strain localization in some loading modes. This result is in contrast to the existing understanding that the SCHAZ might be the site of strain localization.

- Yield stress and tensile stress heterogeneities were observed in all steels with degradation of these properties in the softened HAZ (both SCHAZ and ICHAZ). The heterogeneity in these softened regions increased in higher-strength steels with a higher fraction of martensite in their microstructure.
- Discontinuous yielding in the form of yield point phenomena with corresponding Lüders band was observed in SCHAZ of all steels. The Lüders strain in each steel increased with the peak temperature and was related to the carbon content of the tempered martensite. The magnitude of the Lüders strain was shown to be inversely related to the carbon content of martensite.
- The formation of Lüders band and its propagation was different in different steels. In higher-strength steels, more initiation sites and cross-width propagation were observed.
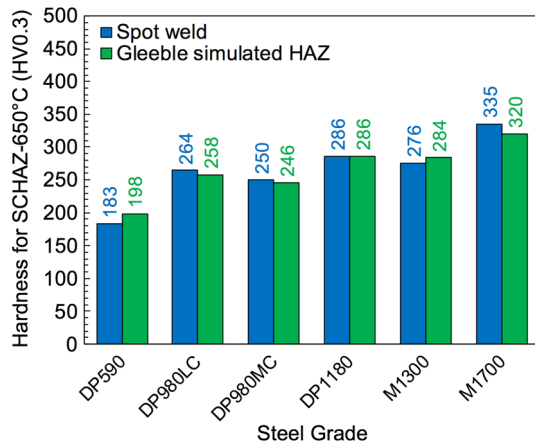
Acknowledgements

Figure 17 Comparison between hardness values from Gleeble thermal simulation for 650 °C peak temperature (as an instance) and softest region of HAZ in all the steels shows only slight differences that are within the uncertainty of indenter locations (± 200 μm) and hardness measurements (± 10 HV).

and John Bohling for the help in setting up the Gleeble simulator for thermal simulations.

Compliance with ethical standards

Conflict of interest The authors declare that they have no conflict of interest.

Appendix

Calibration of Gleeble thermal cycles using hardness values

The calibration of thermal cycles for Gleeble simulations were performed by using hardness measurements. This ensured that the final microstructure is similar to that of the spot weld for the corresponding peak temperature. Results from this step are shown in Fig. 17 for peak temperature of 650 °C.
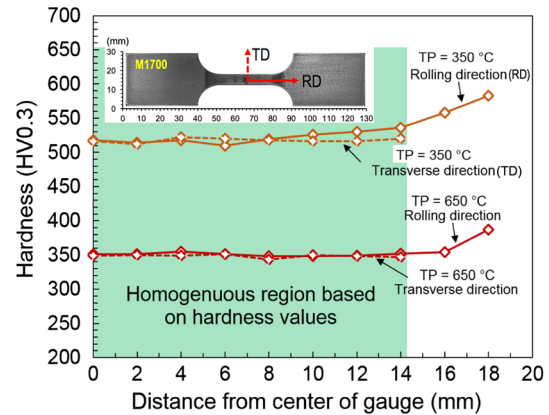

Figure 18 Measured hardness distribution in M1700 sample subjected to thermal simulation with 350 °C and 650 °C peak temperatures along two different directions confirms the validity of our approach to using Gleeble samples as a surrogate to extract constitutive properties of HAZ regions.

Microhardness measurements were also used to check the uniformity of material in the gauge length of tensile samples. Typical results are presented for M1700 samples subjected to two tempering temperatures of 350 and 650 °C presented in Fig. 18, which illustrates a uniform distribution of hardness in both rolling and transverse directions. These results proved the validity of our approach to using Gleeble® simulated samples to extract the stress–strain behavior of spot-welded HAZ regions.

Plastic flows

The methodology for extracting these curves from tensile testing and DIC raw data is explained in "Experimental procedure" section. These results are presented in Fig. 19, in the form of engineering stress–strain curves and for the readers' review.

Figure 19 Engineering stress–strain curves obtained from tensile testing of base metal and Gleeble simulated HAZ samples for all six grades of DP and martensitic AHSS used in this study.
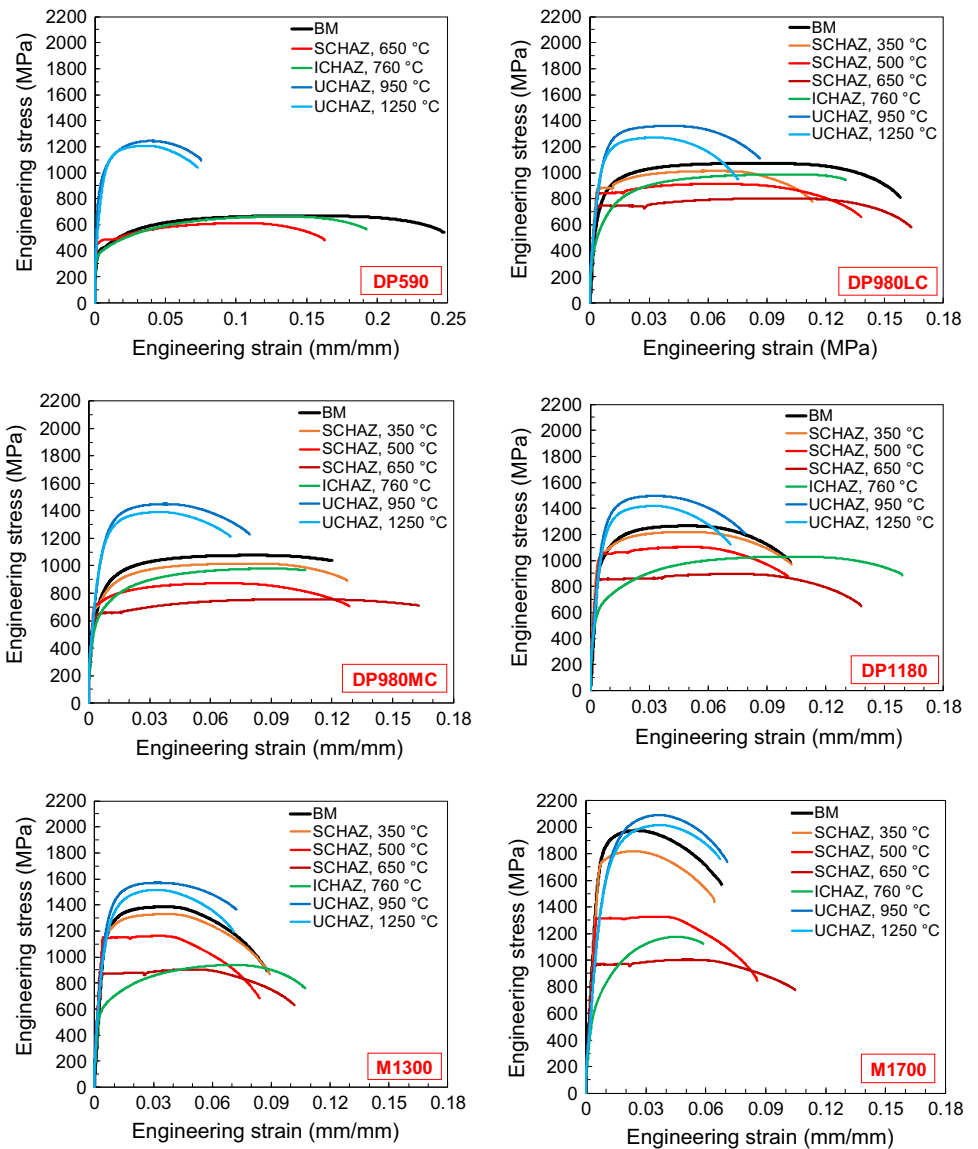
References

[1] Kuziak R, Kawalla R, Waengler S (2008) Advanced high strength steels for automotive industry. Arch Civ Mech Eng 8:103–117

[2] Khan MI, Kuntz ML, Biro E, Zhou Y (2008) Microstructure and mechanical properties of resistance spot welded advanced high strength steels. Mater Trans 49:1629–1637

[3] Dancette S, Massardier-Jourdan V, Fabrègue D, Merlin J, Dupuy T, Bouzekri M (2011) HAZ microstructures and local mechanical properties of high strength steels resistance spot welds. ISIJ Int 51:99–107

[4] Kunishige K, Yamauchi N, Taka T, Nagao N (1983) Softening in weld heat affected zone of dual phase steel sheet for automotive wheel rim, SAE Technical Paper 1983

[5] Biro E, McDermid JR, Embury JD, Zhou Y (2010) Softening kinetics in the subcritical heat-affected zone of dual-phase steel welds. Metall Mater Trans A 41:2348–2356

[6] Baltazar Hernandez VH, Panda SK, Okita Y, Zhou NY (2009) A study on heat affected zone softening in resistance spot welded dual phase steel by nanoindentation. J Mater Sci 45:1638–1647. https://doi.org/10.1007/s10853-009-4141-0

[7] Waterschoot T, Verbeken K, De Cooman BC (2006) Tempering kinetics of the martensitic phase in DP steel. ISIJ Int 46:138–146

[8] Xia M, Biro E, Tian Z, Zhou YN (2008) Effects of heat input and martensite on HAZ softening in laser welding of dual phase steels. ISIJ Int 48:809–814

[9] Speich GR (1981) Physical metallurgy of dual-phase steels. In: Fundamentals of dual-phase steels, pp 3–45

[10] Rezayat H, Babu SS, Ghassemi-Armaki H (2016) Effects of heat affected zone softening extent on strength of advanced high strength steels resistance spot weld. In: Trends in welding research, proceedings of the 10th international conference, Tokyo, Japan

[11] Hernandez VHB, Panda SK, Kuntz ML, Zhou Y (2010) Nanoindentation and microstructure analysis of resistance spot welded dual phase steel. Mater Lett 64:207–210

[12] Baltazar Hernandez VH, Nayak SS, Zhou Y (2011) Tempering of martensite in dual-phase steels and its effects on softening behavior. Metall Mater Trans A 42:3115–3129

[13] Bhadeshia HKDH (1997) Martensite and bainite in steels : transformation mechanism & mechanical properties. Le J Phys IV 07:C5-367–C5-376

[14] Porter DA, Easterling KE, Sherif M (2011) Phase transformations in metals and alloys (Revised Reprint). CRC Press, Boca Raton

[15] Rosenthal D (1941) Mathematical theory of heat distribution during welding and cutting. Weld J 20:220s–234s

[16] Ranganathan BN, Grenga HE (1973) Field-ion microscope investigations of fine structures in as-quenched and tempered ferrous martensite. Scr Metall 7:69–71

[17] Krauss G, Pitsch W (1965) Fine structure and habit planes of martensite in an iron-33 wt (nickel single crystal. J Met 17:1060

[18] Krauss G, Balliett TA (1976) Fine structure and the early stages of tempering in the martensite of an Fe-1.22 C alloy. Metall Trans A 7:318–320

[19] Speich GR, Miller RL (1980) Tempering of ferrite–martensite steels. J Met 32:45–46

[20] Krauss G (2017) Tempering of lath martensite in low and medium carbon steels: assessment and challenges. Steel Res Int 88:1700038

[21] Babu SS, Hono K, Sakurai T (1994) Atom probe field ion microscopy study of the partitioning of substitutional elements during tempering of a low-alloy steel martensite. Metall Mater Trans A 25:499–508

[22] Ghassemi-Armaki H, Biro E, Sadagopan S (2017) Advanced characterization of HAZ softening of AHSS for crash modeling. ISIJ Int 57:1451–1460

[23] Ghassemi-Armaki H, Bhat S, Kelley S, Sadagopan S (2017) Quasi-static spot weld strength of advanced high-strength sheet steels this study highlights the spot weld strength in tension–shear and cross-tension loading modes, and HAZ strength as a function of base metal strength, in sheet steels. Weld J 96:104S–112S

[24] Yang YP, Babu SS, Orth F, Peterson W (2008) Integrated computational model to predict mechanical behaviour of spot weld. Sci Technol Weld Join 13:232–239

[25] AWS D8.9M (2012) Test methods for evaluating the resistance spot welding behavior of automotive sheet steel materials, 3rd edn. American Welding Society (AWS), Miami

[26] Vitek JM, Babu SS (2011) Multiscale characterisation of weldments. Sci Technol Weld Join 16:3–11

[27] Speich GR (1969) Tempering of low-carbon martensite. Trans Metall Soc AIME 245:2553–2564

[28] Morito S, Adachi Y, Ohba T (2009) Morphology and crystallography of sub-blocks in ultra-low carbon lath martensite steel. Mater Trans 50:1919–1923

[29] Biro E, McDermid JR, Vignier S, Norman Zhou Y (2014) Decoupling of the softening processes during rapid tempering of a martensitic steel. Mater Sci Eng A 615:395–404

[30] Saha DC, Biro E, Gerlich AP, Zhou NY (2016) Fusion zone microstructure evolution of fiber laser welded press-hardened steels. Scr Mater 121:18–22

[31] Krauss G, Balliett TA (1976) Fine-structure and early stages of tempering in martensite of an Fe 1.22 C alloy. Metall Trans A Phys Metall Mater Sci 7:318–320

[32] Caron RN, Krauss G (1972) Tempering of Fe–C lath martensite. Metall Trans 3:2381–2389

[33] Hollomon JH, Jaffe LD (1945) Time-temperature relations in tempering steel. Trans Am Inst Min Metall Eng 162:223–249

[34] Ziaebrahimi F, Krauss G (1983) The evaluation of tempered martensite embrittlement in 4130-steel by instrumented Charpy V-notch testing. Metall Trans A Phys Metall Mater Sci 14:1109–1119

[35] Mittemeher EJ, Cheng L, Van der Schaaf PJ, Brakman CM, Korevaar BM (1988) Analysis of nonisothermal transformation kinetics; tempering of iron–carbon and iron–nitrogen martensites. Metall Trans A 19:925–932

[36] Owen WS (1954) The effect of silicon on the kinetics of tempering. Trans Am Soc Met 46:812–829

[37] Wang Y, Denis S, Appolaire B, Archambault P (2004) Modelling of precipitation of carbides during tempering of martensite. J Phys IV (Proc) 120:103–110

[38] Malheiros LRC, Rodriguez EAP, Arlazarov A (2017) Mechanical behavior of tempered martensite: characterization and modeling. Mater Sci Eng A Struct Mater Prop Microstruct Process 706:38–47

[39] Li M, Sun FW, Barrett RA, Meade E, Li DF, O'Donoghue PE et al (2017) Influence of material inhomogeneity on the mechanical response of a tempered martensite steel. Proc Inst Mech Eng Part L J Mater-Des Appl 231:14–22

[40] Bhadeshia HKDH, Honeycombe RWK (2017) Tempering of martensite. In: Steels: microstructure and properties, 4th edn, pp 237–270

[41] Saha DC, Biro E, Gerlich AP, Zhou Y (2016) Effects of tempering mode on the structural changes of martensite. Mater Sci Eng A Struct Mater Prop Microstruct Process 673:467–475

[42] Shi ZM, Gong W, Tomota Y, Harjo S, Li J, Chi B et al (2015) Study of tempering behavior of lath martensite using in situ neutron diffraction. Mater Charact 107:29–32

[43] Li H, Gao S, Tian Y, Terada D, Shibata A, Tsuji N (2015) Influence of tempering on mechanical properties of ferrite and martensite dual phase steel. Mater Today Proc 2:667–671

[44] Cvetkovski K, Ahlstrom J, Persson C (2014) Rapid thermomechanical tempering of iron–carbon martensite. Mater Sci Technol 30:1832–1834

[45] Kang S, Lee SJ (2014) Prediction of tempered martensite hardness incorporating the composition-dependent tempering parameter in low alloy steels. Mater Trans 55:1069–1072

[46] Ohlund CEIC, Schlangen E, Offerman SE (2013) The kinetics of softening and microstructure evolution of martensite in Fe–C–Mn steel during tempering at 300 °C. Mater Sci Eng A Struct Mater Prop Microstruct Process 560:351–357

[47] Sun L, Zhao ZY, Yang XZ, Xue RD (2013) Effect of tempering process on residual stress in hot rolled low carbon martensite high-strength steel strip. Mater Des Process Appl Parts 1–4 690–693:222–226

[48] Di Schino A, Alleva L, Guagnelli M (2012) Microstructure evolution during quenching and tempering of martensite in a medium C steel. Recryst Grain Growth IV 715–716:860–865

[49] Hernandez VHB, Nayak SS, Zhou Y (2011) Tempering of martensite in dual-phase steels and its effects on softening behavior. Metall Mater Trans A Phys Metall Mater Sci 42a:3115–3129

[50] Mazur J (1949) Structure of tempered martensite. Nature 164:230–231

[51] Michel A (1946) The structure of tempered martensite. J Iron Steel Inst 154:P152–P153

[52] Cottrell AH, Bilby BA (1949) Dislocation theory of yielding and strain ageing of iron. Proc Phys Soc Lond Sect A 62:49–62

[53] Hall E (2012) Yield point phenomena in metals and alloys. Springer, Berlin

[54] Waterschoot T, De AK, Vandeputte S, De Cooman BC (2003) Static strain aging phenomena in cold-rolled dual-phase steels. Metal Mater Trans A Phys Metall Mater Sci 34a:781–791

[55] Ahn TH, Oh CS, Lee K, George EP, Han HN (2012) Relationship between yield point phenomena and the nanoindentation pop-in behavior of steel. J Mater Res 27:39–44

[56] Conrad H, Schoeck G (1960) Cottrell locking and the flow stress in iron. Acta Metall 8:791–796

[57] Gerberich WW, Venkataraman S, Nelson J, Huang H, Lilleodden E, Bonin W (1995) Yield point phenomena and dislocation velocities underneath indentations into BCC crystals. Thin Films Stress Mech Prop V 356:629–644

[58] Hahn GT (1962) Model for yielding with special reference to yield-point phenomena of iron and related bcc metals. Acta Metall 10:727–738

[59] Tsuchida N, Tomota Y, Nagai K, Fukaura K (2006) A simple relationship between Luders elongation and work-hardening rate at lower yield stress. Scr Mater 54:57–60